

DESIGN AND MODELING OF A BIOMIMETIC ROBOTIC WRIST VIA HYBRID MECHANISM

Mohammed El Kihal, Jiamin Wang, Oumar Barry*
 Department of Mechanical Engineering
 Virginia Polytechnic Institute and State University
 Blacksburg, Virginia 24061

ABSTRACT

The wrist is critical to people's activities of daily living, which consists of two major degrees of freedom (DOF) - flexion-extension (FE) and radial-ulnar-deviation (RUD). This paper proposes a novel 2-DOF biomimetic robotic wrist design for a forearm mannequin, which is developed as a safe test bench that emulates human forearm movements for exoskeleton experimentation. Due to the complexity of the coupled motions of FE and RUD, existing robotic wrists mainly focus on the FE motion, and sometimes incorporate the forearm pronation/supination instead of the RUD motion. To solve this issue, the robotic wrist features a simple but effective hybrid mechanism for FE and RUD motions, which avoids the axes offset between FE and RUD from producing unnatural wrist movements and allows ranges of motions comparable to those in a human wrist. We analyze the kinematics of the hybrid wrist mechanism, which leads to the establishment of the dynamical model through a generic constrained multibody formulation. A robust controller is then adopted for reference trajectory tracking control. We then perform numerical simulations, which validate the control performance and actuator choice, and evaluate the workspace, rotation axes offset, and inertial characteristics. The results preliminarily verify the biomimetic robotic wrist as a feasible solution for the forearm mannequin to realize natural wrist movement emulation.

NOMENCLATURE

The mathematical notations used are listed as follows:

$\|\mathbf{Z}\|_n$ n -norm of a matrix \mathbf{Z} ($n = 2$ if not specified)

\mathbf{c}_m $m \times 1$ vector whose elements equal to $\mathbf{c} \in \mathbb{R}$

$\mathbf{c}_{m \times n}$ $m \times n$ matrix whose elements equal to $\mathbf{c} \in \mathbb{R}$ (m, n fit with neighboring blocks if not specified)

\mathbf{I}_n Identity matrix of dimension n (n fits with neighboring blocks if not specified)

\mathbf{Z}^{-T} Transposed inverse of \mathbf{Z} (since $(\mathbf{Z}^{-1})^T = (\mathbf{Z}^T)^{-1}$)

$\mathbf{Z} > 0$ A square matrix \mathbf{Z} is positive definite

\mathbf{Z}^+ The Moore-Penrose pseudoinverse of \mathbf{Z}

$\text{diag}(\underline{\mathbf{z}})$ Convert a vector $\underline{\mathbf{z}}$ into a diagonal matrix, whose diagonal elements are the elements of $\underline{\mathbf{z}}$

1 INTRODUCTION

The wrist is a crucial biomechanical joint for humans to perform manipulations. As illustrated in Fig. 1, the wrist possesses a complicated skeletal structure and two major degrees of freedom (DOF) - flexion/extension (FE) and radial/ulnar deviation (RUD) [1]. Previous studies show that the ranges of motion of FE and RUD are respectively $[-75^\circ, 75^\circ]$ (from flexion to extension) and $[-45^\circ, 29^\circ]$ (from ulnar to radial deviation) [1–3]. Also, FE and RUD are coupled motions, and the approximate rotation axes of FE and RUD can shift translationally and rotationally during wrist movements [4, 5].

Inspired by nature, many humanoid and prosthetic designs feature multi-DOF joints that resemble the wrist for end effector

*Corresponding Author (Email: obarry@vt.edu)

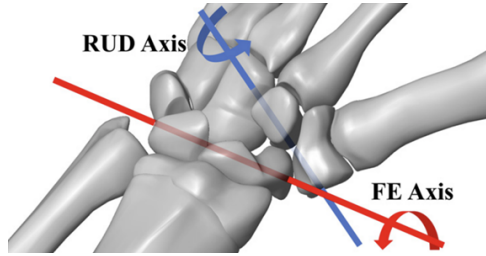


FIGURE 1: THE WRIST SKELETAL MODEL ON A LEFT HUMAN FOREARM AND APPROXIMATE LOCATIONS OF THE FE AND RUD AXES.

rotations. Existing works adopt serial [6–9], parallel [10–13], and hybrid [14, 15] mechanisms. Most of these mechanisms are driven by rotary electric motors [6, 7, 10–15], while others also employ hydraulics/pneumatic tendon actuators [16–19]. In general, serial mechanisms provide better ranges of motion than parallel ones. However, serial mechanisms may also suffer from larger axes offsets, reducing their resemblance to the human wrist.

Our team is developing a robotic forearm mannequin as a safe test bench for upper-limb exoskeleton experimentation [20]. The mannequin is required to be biomimetic in geometry and kinematics so that it can emulate the movements of a human forearm. In addition to kinematic likeness, existing robotic wrists often lack compactness and range of motion. Many 2-DOF robotic wrist designs also neglect the RUD motion by focusing on FE and forearm pronation/supination (PS) instead, since it is easier to set up FE and PS joints in series with no axis offset. As a result, very few robotic wrists feature FE and RUD with adequate ranges of motion and small axes offsets.

This paper proposes a novel 2-DOF robotic wrist. The design features a simple but effective hybrid mechanism for FE and RUD motions, which avoids the axes offset between FE and RUD from producing unnatural wrist movements, and allows ranges of motions comparable to those in a human wrist. The rest of the paper is arranged as follows. The design, mechanism, and kinematics of the wrist are introduced in Section 2. We then discuss the dynamical modeling and controller design for the exoskeleton in Section 3 and present the dynamical properties through numerical simulations in Section 4. Finally, the findings in this work are summarized in Section 5.

2 The Wrist Design and Its Kinematics

The robotic wrist proposed in this paper adopts a simple but effective 2-DOF hybrid mechanism for RUD and FE motions. The forearm mannequin featuring the robotic wrist is overviewed in Fig. 2, where the design aims to closely resemble a human forearm. The details of the robotic wrist are shown in Fig. 3. The 2-DOF hybrid mechanism is actuated by two servo motors (Dynamixel XM430-W210). The first DOF on the RUD direction is



FIGURE 2: OVERVIEW OF THE FOREARM MANNEQUIN FEATURING THE PROPOSED ROBOTIC WRIST.

realized by the motor installed at the distal forearm base. The second DOF in the FE direction is driven by the motor installed at the hand base. While the RUD rotation is straightforwardly along the axis of the RUD servomotor, the FE rotation is composed of two separate but constrained rotations. The first passive rotation takes place along the joint connecting the side links (which moves together) and the motor frame and the second active rotation occurs along the motor axis. The coupling of the two rotations is realized with the paralleling pair of straight teeth gears integrated into the motor frames. The gear ratio determines the relationship of the rotations. In the current design, the gear ratio is 1:1, which equalizes the two coupled rotations. Note that the separation of FE rotation is also inspired by the radiocarpal and midcarpal joints in the human wrist [21,22], which both contribute to the wrist rotations.

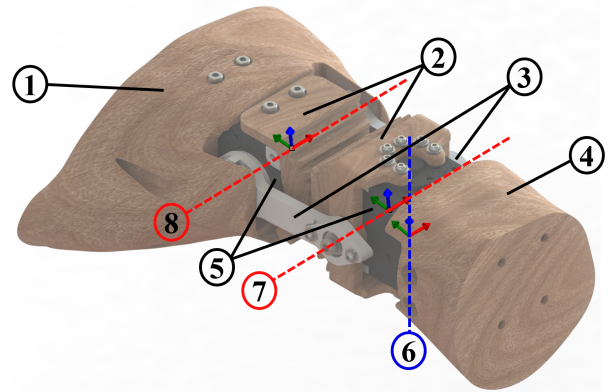


FIGURE 3: THE DESIGN OF THE ROBOTIC WRIST ON THE RIGHT FOREARM. 1: HAND BASE; 2: MOTOR FRAMES WITH STRAIGHT TEETH GEARS; 3: SIDE LINKS; 4: DISTAL FOREARM BASE; 5: SERVO MOTORS; 6: RUD MOTOR AXIS; 7: FE BEARING AXIS; 8: FE MOTOR AXIS

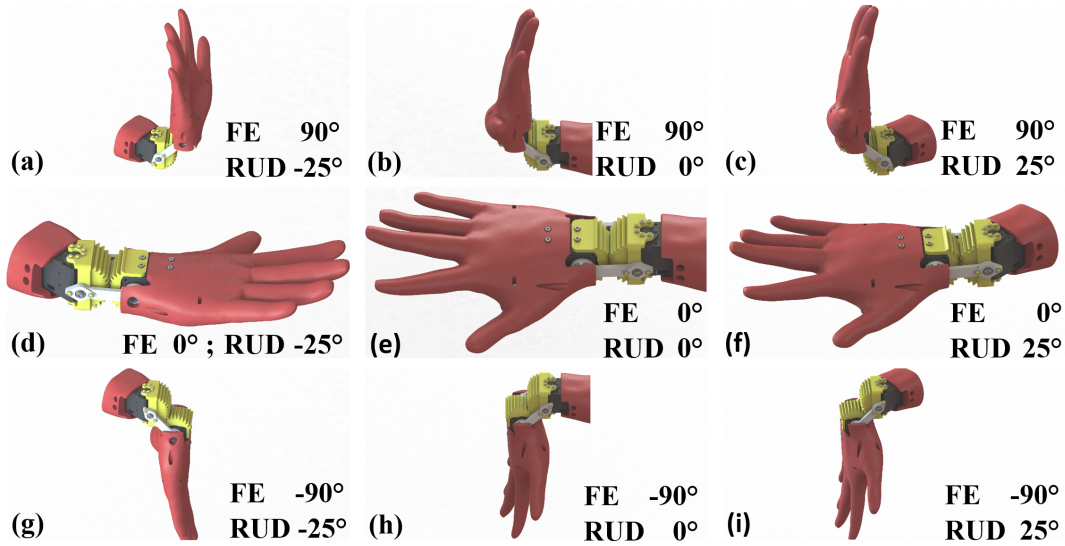


FIGURE 4: WRIST MANNEQUIN AT ROTATION LIMITS

The hybrid mechanism design allows the robotic wrist to be compact and reach the ranges of motion in FE and RUD close to that in a human wrist. With the structural components made from plastics, the weight of the assembly shown in Fig. 3 is approximately 348 grams and can be further adjusted to match the human anatomy. The robotic wrist can reach $[-90^\circ, 90^\circ]$ from flexion to extension, and $[-25^\circ, 25^\circ]$ from ulnar to radial deviation, which is demonstrated in Fig. 4.

In robotic wrist designs that adopt the universal joint mechanism, the offset between the FE and RUD rotations can be determined by the size of in-line motors. The offset can increase along with the size of the motor. When the offset is large, extreme FE rotations can result in the proximal end of the hand “sinking” into the distal end of the forearm, which does not resemble the behavior of a human wrist [23]. The proposed mechanism prevents this

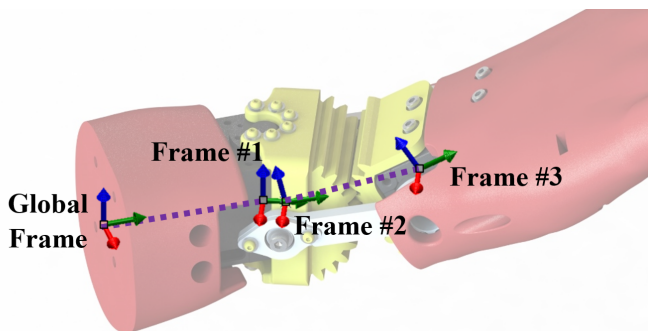


FIGURE 5: COORDINATE FRAMES OF THE MANNEQUIN WRIST SYSTEM (RED ARROW: X-AXIS; GREEN ARROW: Y-AXIS; BLUE ARROW: Z-AXIS).

TABLE 1: PROPERTIES OF HOMOGENEOUS TRANSFORMATIONS BETWEEN COORDINATE FRAMES, WHERE THE NUMERICAL VALUES ARE THE DEFAULT DESIGN PARAMETERS OF THE ROBOTIC WRIST

From	To	Translation (d)	Rotation (R)
G	#1	$d_{y,1} = 4.94$ cm	$R_{z,1}(\mathbf{q}_1)$
#1	#2	$d_{y,2} = 0.70$ cm	$R_{x,2}(\mathbf{q}_2)$
#2	#3	$d_{y,3} = 4.49$ cm	$R_{x,3}(\mathbf{q}_3)$

problem. As the FE motion is separated into two parts, the hand will translate while rotating with respect to the distal end of the forearm. As shown in Fig. 4, the hand moves downward/upward with respect to the forearm during flexion/extension. Hence, the FE rotation does not have a fixed axis. In the current design, the offset between the approximate FE and RUD axes shifts between 1.7-2.9 cm during FE and RUD movements.

The kinematic frames of the robotic wrist are presented in Fig. 5, where the forearm base is fixed to the global frame, Frame 1 is placed at the forearm servomotor frame after the RUD rotation, Frame 2 is fixed to the side links after the half FE rotation, and Frame 3 is located at the hand after full FE rotation. Here, with respect to the global frame, the RUD rotation axis approximately aligns with the z -axis, and the FE rotation axis approximately aligns with the x -axis. With the homogeneous transformation matrix $\mathbf{T}_{i,j}$ (from frame # i to frame # j) as

$$\mathbf{T}_{i,j} = \begin{bmatrix} \mathbf{R}_{i,j} & \mathbf{d}_{i,j} \\ \mathbf{0}_{1 \times 3} & 1 \end{bmatrix} = \mathbf{T}_{j,i}^{-1}, \quad \mathbf{T}_{j,i} = \begin{bmatrix} \mathbf{R}_{i,j}^T & -\mathbf{R}_{i,j}^T \mathbf{d}_{i,j} \\ \mathbf{0}_{1 \times 3} & 1 \end{bmatrix} \quad (1)$$

where $\mathbf{R} \in \mathbb{R}^{3 \times 3}$ and $\mathbf{d} \in \mathbb{R}^3$ are respectively the rotation matrix and translational displacement, the transformation from the global frame to Frame 3, can be calculated as

$$\mathbf{T}_{G,3} = \mathbf{T}_{G,1} \mathbf{T}_{1,2} \mathbf{T}_{2,3} \quad (2)$$

For this design, the kinematic parameters between transformations are listed in Tab. 1. The generalized coordinate \mathbf{q}_0 of the system is defined as $\mathbf{q}_0 = [q_1, q_2, q_3]^T$, where the q_1 is the forearm servomotor angle, q_2 is the passive joint angle, and q_3 is the hand servomotor angle. Hence, with the kinematic properties of the robotic wrist calculated, we can perform the dynamical modeling and controller design of the forearm mannequin, which are discussed in the next section.

3 Dynamical Model and Control

With the design and kinematics of the robotic wrist explained in the previous section, the next step is to design a proper motion controller to perform trajectory tracking of the wrist. This requires the establishment of a multibody dynamical model for the forearm mannequin. A general multibody model can be written in the form of

$$\mathbf{M}(\mathbf{q})\ddot{\mathbf{q}} + \mathbf{C}(\mathbf{q}, \dot{\mathbf{q}})\dot{\mathbf{q}} + \mathbf{h}(t, \mathbf{q}, \dot{\mathbf{q}}) = \mathbf{J}_u(\mathbf{q})^T \mathbf{u} \quad (3)$$

where \mathbf{q} is the generalized coordinate, \mathbf{M} is the inertia matrix, \mathbf{C} is the Coriolis and centripetal (CC) matrix, \mathbf{h} is the generalized system force, \mathbf{u} is the control input, and \mathbf{J}_u is the input Jacobian.

Here, it should be pointed out that \mathbf{q} is assumed to contain only independent coordinates. In this work, with the linkage-gear coupling, we can obtain $q_2 = q_3$, so that $\mathbf{q} = [q_1, q_2]^T$. However, it should be noted that the adopted mechanism is not unique to realize the designed wrist kinematics. Hence, we derive the dynamical model via a more general approach.

3.1 Multibody Dynamics and Constraints

The multibody model is developed based on Kane's method [24]. For each coordinate frame, we can derive the frame Jacobian matrix $\mathbf{J}_i \in \mathbb{R}^{6 \times 2}$ as

$$\mathbf{J}_i = [\mathbf{J}_{i,\omega}^T \quad \mathbf{J}_{i,d}^T]^T \quad (4)$$

where $\mathbf{J}_{i,d} \in \mathbb{R}^{3 \times 2}$ and $\mathbf{J}_{i,\omega} \in \mathbb{R}^{3 \times 2}$ corresponds to the translation and rotation Jacobians, respectively, so that

$$\dot{\mathbf{d}} = \mathbf{J}_{i,d}\dot{\mathbf{q}}; \quad \boldsymbol{\omega} = \mathbf{J}_{i,\omega}\dot{\mathbf{q}} \quad (5)$$

where \mathbf{d} is the global translational displacement, and $\boldsymbol{\omega}$ is the angular velocity in the global frame. By defining $\mathbf{R}_{G,i}$ as the rotation matrix from the global frame to Frame i , with m_i and Φ_i respectively as the mass and inertia moment of a body defined at Frame i , the inertia matrix \mathbf{M}_i in the global frame can be calculated as

$$\mathbf{M}_i = \mathbf{J}_i^T \begin{bmatrix} \mathbf{R}_{G,i} \Phi_i \mathbf{R}_{G,i}^T & \mathbf{0}_{3 \times 3} \\ \mathbf{0}_{3 \times 3} & m_i \mathbf{I}_3 \end{bmatrix} \mathbf{J}_i \quad (6)$$

and the CC matrix can be written as

$$\mathbf{C}_i = \mathbf{J}_i^T \begin{bmatrix} \mathbf{R}_{G,i} \Phi_i \mathbf{R}_{G,i}^T & \mathbf{0}_{3 \times 3} \\ \mathbf{0}_{3 \times 3} & m_i \mathbf{I}_3 \end{bmatrix} \mathbf{J}_i + \mathbf{J}_{i,\omega}^T \mathbf{R}_{G,i} \Phi_i \dot{\mathbf{R}}_{G,i}^T \mathbf{J}_i \boldsymbol{\omega} \quad (7)$$

The sum of individual inertial properties leads to the total inertial matrix \mathbf{M}_0 and CC matrix \mathbf{C}_0 as

$$\mathbf{M}_0 = \sum_{i=1}^n \mathbf{M}_i; \quad \mathbf{C}_0 = \sum_{i=1}^n \mathbf{C}_i \quad (8)$$

The generalized force \mathbf{h}_0 in the system consists of gravitational loads, potential energy forces, and damping. As an example, by assuming that the z -axis of the global frame is the vertical axis, the gravitational load of the body on frame i can be written as

$$\mathbf{h}_{g,i} = -\mathbf{J}_{i,z}^T m_i g \quad (9)$$

where $\mathbf{J}_{i,z}$ is the third row of \mathbf{J}_i . Hence, the multibody system can be written as

$$\mathbf{M}_0 \ddot{\mathbf{q}}_0 + \mathbf{C}_0 \dot{\mathbf{q}}_0 + \mathbf{h}_0 = \mathbf{J}_{u,0}^T \mathbf{u} + \mathbf{J}_{\lambda,0}^T \lambda \quad (10)$$

where λ is the Lagrange multiplier serving as the constraint force, and $\mathbf{J}_{\lambda,0}$ is the constraint Jacobian calculated from the kinematic constraints

$$\dot{\mathbf{r}}_\lambda = \mathbf{J}_\lambda(\mathbf{q})\dot{\mathbf{q}} = 0 \quad (11)$$

By defining that

$$\mathbf{q}_0 = [\mathbf{q}^T \quad \mathbf{q}_c^T]^T \quad (12)$$

where \mathbf{q}_c is the dependent generalized coordinates, we can obtain

$$\mathbf{J}_\lambda = [\mathbf{J}_{\lambda,i} \quad \mathbf{J}_{\lambda,c}] \quad (13)$$

with $\mathbf{J}_{\lambda,i}$ corresponding to \mathbf{q} , and $\mathbf{J}_{\lambda,c}$ corresponding to \mathbf{q}_c . If $\mathbf{J}_{\lambda,c}$ is invertible, we can reduce the order of the model by obtaining

$$\dot{\mathbf{q}}_c = -\mathbf{J}_{\lambda,c}^{-1} \mathbf{J}_{\lambda,i} \dot{\mathbf{q}} \quad (14)$$

so that

$$\mathbf{B} = \begin{bmatrix} \mathbf{I}_i \\ -\mathbf{J}_{\lambda,c}^{-1} \mathbf{J}_{\lambda,i} \end{bmatrix}; \quad \dot{\mathbf{q}}_0 = \mathbf{B} \dot{\mathbf{q}} \quad (15)$$

Hence, we can obtain the final model written in Eq. (3) with the dynamical properties calculated as

$$\mathbf{M} = \mathbf{B}^T \mathbf{M}_0 \mathbf{B}; \quad \mathbf{C} = \mathbf{B}^T \mathbf{M}_0 \dot{\mathbf{B}}^T + \mathbf{B}^T \mathbf{C}_0 \mathbf{B} \quad (16a)$$

$$\mathbf{h} = \mathbf{B}^T \mathbf{h}_0; \quad \mathbf{J}_u^T = \mathbf{B}^T \mathbf{J}_{0,u}^T \quad (16b)$$

In this study, recall that $\mathbf{q}_0 = [q_1, q_2, q_3]^T$ is the original generalized coordinate. Based on the constraint $\mathbf{r}_\lambda = q_2 - q_3 = 0$, we obtain $\mathbf{q} = [q_1, q_2]^T$, where $+q_1$ as radial deviation direction, $-q_1$ as ulnar deviation direction, $+q_2$ as the extension direction, and $-q_2$ as the flexion direction. The control input $\mathbf{u} = [u_1, u_2]^T$ are the actuation torques provided by the forearm servomotor (RUD) and hand servomotor (FE), respectively.

3.2 Motion Control

This subsection discusses the motion controller used to drive the robotic wrist. First, the tracking error $\boldsymbol{\varepsilon} \in \mathbb{R}^{n_q}$ defined by the time-dependent tracking reference $\mathbf{r} \in \mathbb{R}^{n_2}$, and the control system state $\mathbf{x} \in \mathbb{R}^{n_4}$ are respectively defined as

$$\boldsymbol{\varepsilon} = \mathbf{q} - \mathbf{r}; \quad \mathbf{x} = [\boldsymbol{\varepsilon}^T \ \dot{\boldsymbol{\varepsilon}}^T]^T \quad (17)$$

Here, we assume that the tracking reference \mathbf{r} is smooth, bounded, and directly available. The control system can then be written as

$$\dot{\mathbf{x}} = \mathbf{f}(\mathbf{x}) + \mathbf{g}(t, \mathbf{q}, \dot{\mathbf{q}}) + \mathbf{U}(\mathbf{q})\mathbf{u} \quad (18)$$

where

$$\mathbf{f} = [\dot{\boldsymbol{\varepsilon}} \ \mathbf{0}]^T; \quad \mathbf{g} = [\mathbf{0} \ -\ddot{\mathbf{r}} - \mathbf{M}^{-1}(\mathbf{C}\dot{\mathbf{q}} + \mathbf{h})]^T; \quad \mathbf{U} = [\mathbf{0} \ \mathbf{M}^{-1}\mathbf{J}_u^T]^T \quad (19)$$

which is a time-dependent nonlinear control system affine in \mathbf{u}_c .

The chosen controller is an inverse optimal robust controller based on the work in [25]. The controller can be written as

$$\mathbf{u} = \mathbf{J}_u^{-T}(\mathbf{u}_f(t, \mathbf{q}, \dot{\mathbf{q}}) + \mathbf{u}_b(t, \mathbf{x})) \quad (20)$$

with the feed-forward term $\mathbf{u}_f \in \mathbb{R}^{n_q}$, feedback term $\mathbf{u}_b \in \mathbb{R}^{n_q}$, $\boldsymbol{\xi} \in \mathbb{R}^{n_q}$ and $\boldsymbol{\Omega}(t, \mathbf{x}) \in \mathbb{R}^{n_q \times n_q}$ respectively defined as

$$\mathbf{u}_f = \mathbf{M}\dot{\boldsymbol{\zeta}} + \mathbf{C}\boldsymbol{\zeta} + \mathbf{h}; \quad \mathbf{u}_b = -c_1\boldsymbol{\Omega}^{-1}\boldsymbol{\xi} \quad (21a)$$

$$\boldsymbol{\xi} = \dot{\boldsymbol{\varepsilon}} + \mathbf{K}_1\boldsymbol{\varepsilon}; \quad \boldsymbol{\zeta} = \dot{\mathbf{r}} - \mathbf{K}_1\boldsymbol{\varepsilon} \quad (21b)$$

$$\boldsymbol{\Omega} = (\mathbf{J}_\omega^T\mathbf{J}_\omega + \mathbf{K}_2)^{-1} \quad (21c)$$

where we set $\mathbf{J}_\omega = \mathbf{M}^{1/2}$ to scale the control gains linearly with respect to the inertia. $\mathbf{K}_1, \mathbf{K}_2 \in \mathbb{R}^{2 \times 2}$ are symmetric positive definite gain matrices and $c_1 > 2$. The adopted robust controller in Eq. 20 asymptotically stabilizes the Lyapunov function

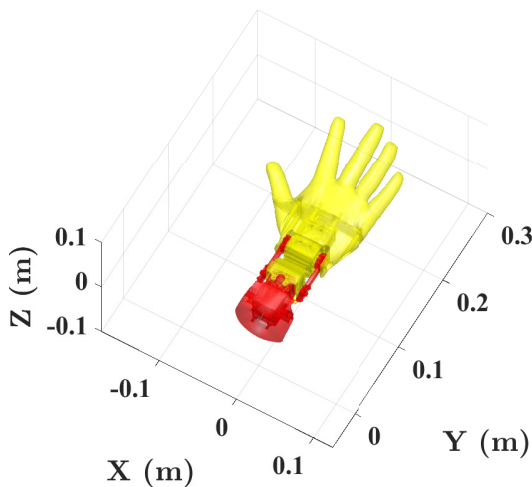


FIGURE 6: THE 3D MODEL OF THE ROBOTIC WRIST MODEL IN THE MATLAB SIMULATION.

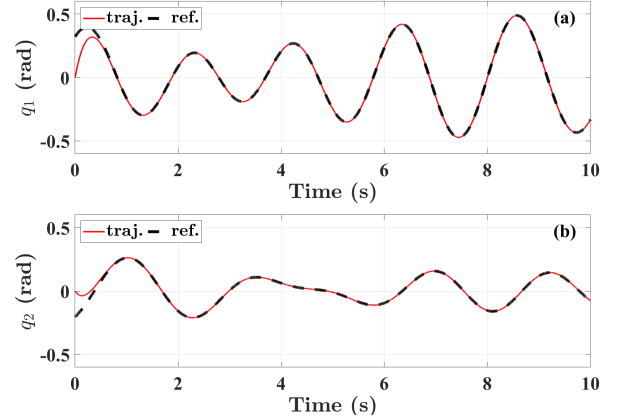


FIGURE 7: THE CONTROL SIMULATION OF THE ROBOTIC WRIST MODEL WHERE (a) AND (b) SHOW THE TRACKING PERFORMANCE OF q_1 AND q_2 , RESPECTIVELY.

$$\mathcal{V}(\mathbf{x}) = \frac{1}{2}\mathbf{x}^T \begin{bmatrix} \mathbf{K}_3 + \mathbf{K}_1\mathbf{M}\mathbf{K}_1 & \mathbf{K}_1\mathbf{M} \\ \mathbf{M}\mathbf{K}_1 & \mathbf{M} \end{bmatrix} \mathbf{x} \quad (22)$$

where $\mathbf{K}_3 \in \mathbb{R}^{2 \times 2}$ is symmetric positive definite. The stability proof is elaborated in [25], and the controller will be used for simulations in the next section.

4 Numerical Analysis

This section presents the numerical analysis of the biomimetic robotic wrist carried out in MATLAB [26], where the 3D visualization of the design is shown in Fig. 6. The first simulation tests the validity of the motion controller in Eq. (20). A set of tracking trajectories is generated based on the combination of random harmonic components ranging from 1 to 2 Hz. The tracking trajectory performance is shown in Fig. 7, where it is observed that the tracking errors quickly converge to the references. The control input required to perform the trajectory tracking is shown in Fig. 8. After the input peaks due to large initial tracking error, the

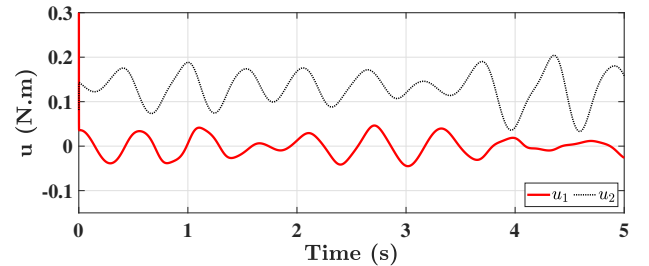


FIGURE 8: THE CONTROL SIMULATION OF THE ROBOTIC WRIST MODEL SHOWING THE TORQUE INPUTS u_1 AND u_2 REQUIRED FOR THE REFERENCE TRACKING.

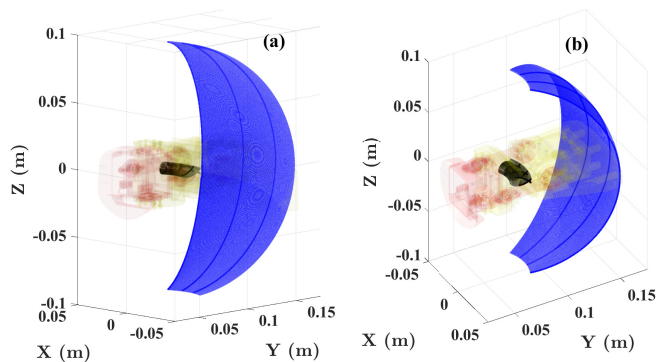


FIGURE 9: WORKSPACE AND FE ROTATION AXIS SURFACE FOR $q_1 \in [-25^\circ, 25^\circ]$ AND $q_2 \in [-45^\circ, 45^\circ]$, WHERE THE BLUE AND THE BLACK SURFACES REPRESENT THE WORKSPACE AND THE FE ROTATION AXIS SURFACE, RESPECTIVELY.

maximum steady-state control inputs are approximately within 0.2 Nm, which is within the capability of the adopted servomotors. Also, notice that the average of the FE servomotor input u_2 is offset above zero since this input is needed to compensate for the gravitational load. This offset will further increase with the extra payload applied to the mannequin.

The workspace and the axis offset of the robotic wrist were observed over the range of q_1 and q_2 . Figure 9 shows the reachable surface (in blue color) of an endpoint on the hand with a 6 cm displacement along the y axis from the FE servomotor axis. The surface appears to be a stretched ellipsoid, which is created from a large concatenated arc from the FE rotation being swept by the RUD rotation. As a result of the 2-DOF hybrid mechanism, the total FE rotation does not have a fixed axis. Hence, we evaluate the reachable surface (in black color) of an arbitrarily point displaced along the y axis by -3 cm from the FE servomotor axis, which is close to the approximate location of the total FE rotation axis. The zoomed-in view in Fig. 10 shows that the surface holds the shape of a loop. This supports the estimation that the RUD-FE axes offset ranges within 1.7-2.9 cm.

We further compared the reachable surfaces of an endpoint

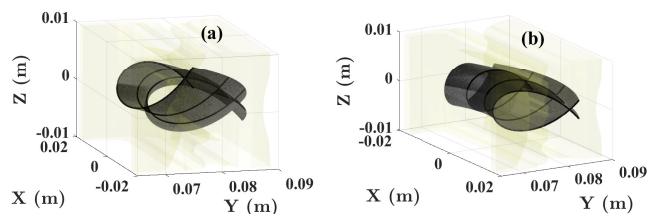


FIGURE 10: CLOSE UP VIEW ON THE FE ROTATION AXIS SURFACE FOR $q_1 \in [-25^\circ, 25^\circ]$ AND $q_2 \in [-45^\circ, 45^\circ]$.

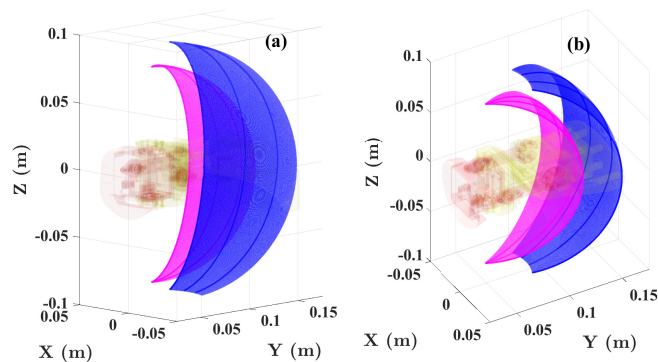


FIGURE 11: WORKSPACE COMPARISON BETWEEN THE PRESENTED NOVEL ROBOTIC WRIST AND AN ALTERNATIVE FOREARM MODEL WITH ZERO AXIS OFFSET

on the hand from the current design, and that from an alternative forearm model where the wrist axis offset is zero, which is shown in Fig. 11. For the alternative forearm model, the displacement of the endpoint is 8 cm along the y axis from the FE servomotor axis. Here, we noticed that without the offset, the magenta surface from the alternative model comes from a standard sphere with a radius of 8 cm. It can also be observed that the blue shape is stretched in the y-direction, as a result of the FE rotation axis moving on the y-direction as q_1 changes within the range $[-25^\circ, 25^\circ]$, and the z-direction, as a result of the FE rotation axis moving on the z-direction as q_2 changes within the range $[-45^\circ, 45^\circ]$.

Finally, we analyzed the eigenvalues of the inertia matrix \mathbf{M} within the workspace. The ratio between the eigenvalue's real parts determines whether the system will be more or less affected

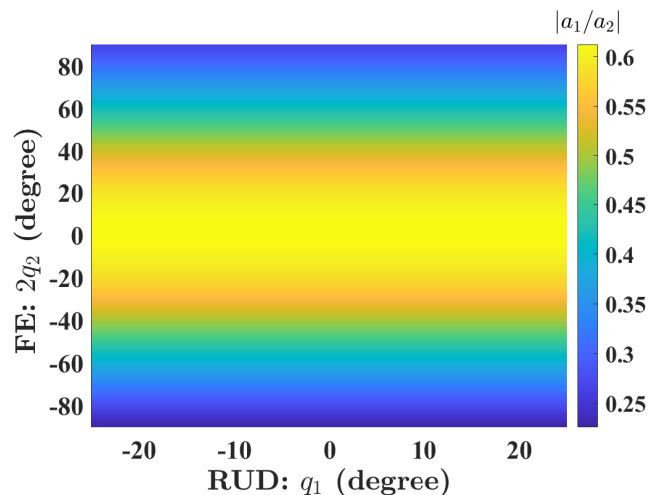


FIGURE 12: INERTIA MATRIX \mathbf{M} EIGENVALUE RATIO COMPARISON FOR $q_1 \in [-25^\circ, 25^\circ]$ AND $q_2 \in [-45^\circ, 45^\circ]$.

by disturbances in one DOF than another. Since \mathbf{M} is a 2×2 matrix, here we define the \mathbf{a} as the eigenvalue vector, and

$$a_1 = \min(|\text{real}(\mathbf{a})|); \quad a_2 = \max(|\text{real}(\mathbf{a})|); \quad (23)$$

Hence, the ratio $|a_1/a_2| = 0$ indicates that the inertial matrix is singular, and $|a_1/a_2| = 1$ indicates that the eigenvalues are complex conjugates. The eigenvalue ratio within the workspace is shown in Fig. 12, which is primarily affected by the FE rotation. Notice that the ratio ranges from 0.25 to 0.6 throughout the workspace, and reaches minimums at extreme flexion and extensions. This is expected since the moment of inertia along the RUD servomotor axis will be minimized when FE is at full rotation $2q_2 = \pm 90^\circ$, at which points the RUD movements can be affected by less torque.

5 Conclusion and Future Work

This paper introduced a novel 2-DOF robotic wrist for biomimetic forearm mannequins used as safe test benches for upper-limb exoskeleton experimentation. The proposed design features a simple but effective hybrid mechanism for FE and RUD motions, which, unlike the previous robotic wrist designs, avoids the axes offset between FE and RUD from producing unnatural wrist movements, and allows ranges of motions comparable to those in a human wrist. The mechanism design was extensively explained along with the modeling of the robotic wrist kinematics. We then established the dynamical model following a general constrained multibody formulation and designed the robust motion controller for trajectory tracking. Through simulations, we demonstrated the validity of the motion controller, as it can rapidly converge the tracking error, and track the reference with the permissible servomotor torque inputs. The multibody model also provided means to evaluate the behavior of the robotic wrist in terms of workspace, axis offset, and inertial properties. The results preliminarily verified the robotic wrist as a feasible solution for the forearm mannequin to realize natural wrist movement emulation.

The proposed robotic wrist has already been prototyped as shown in Fig. 13, which is expected to be used for the early testing of a wearable wrist exoskeleton [20]. For future works, we will investigate other mechanisms that can better emulate the wrist movement, and further develop the mannequin by including the remaining DOFs in the forearm.

REFERENCES

- [1] Boone, D. C., and Azen, S. P., 1979. "Normal range of motion of joints in male subjects". *The Journal of Bone And Joint Surgery*, **61**, pp. 756–759.
- [2] Soucie, J. M., Wang, C., Forsyth, A., Funk, S., Denny, M., Roach, K. E., and Boone, D., 2011. "Range of motion measurements: Reference values and a database for comparison studies". *Haemophilia*, **17**, 5, pp. 500–507.
- [3] Ryu, J., Cooney, W. P., Askew, L. J., An, K. N., and Chao,

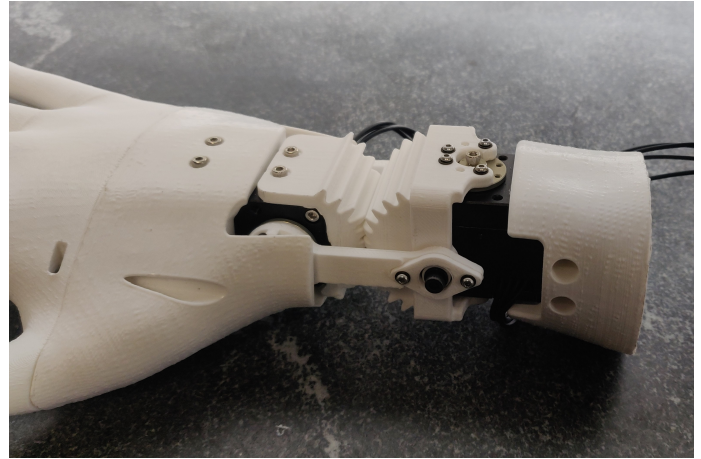


FIGURE 13: ROBOTIC WRIST PROTOTYPE

- E. Y., 1991. "Functional ranges of motion of the wrist joint". *The Journal of Hand Surgery*, **16**, 5, pp. 409–419.
- [4] Moore, D. C., Crisco, J. J., Trafton, T. G., and Leventhal, E. L., 2007. "A digital database of wrist bone anatomy and carpal kinematics". *Journal of biomechanics*, **40**(11), pp. 2537–2542.
- [5] Akhbari, B., Moore, D. C., Laidlaw, D. H., Weiss, A.-P. C., Akelman, E., Wolfe, S. W., and Crisco, J. J., 2019. "Predicting carpal bone kinematics using an expanded digital database of wrist carpal bone anatomy and kinematics". *Journal of Orthopaedic Research®*.
- [6] Razak, N. A. A., Osman, N. A. A., Gholizadeh, H., and Ali, S., 2014. "Development and performance of a new prosthesis system using ultrasonic sensor for wrist movements: A preliminary study". *BioMedical Engineering Online*, **13**, 4, pp. 1–14.
- [7] Fan, S., Fan, S., Jiang, L., and Liu, H., 2016. "A design of a miniaturized prosthetic wrist based on repetition rate of human wrist daily tasks". *2016 IEEE International Conference on Robotics and Biomimetics, ROBIO 2016*, pp. 1643–1648.
- [8] NATSUME, T., 2015. "All purpose humanoid robot for life science—a new dimension to lab automation—". *Journal of The Japanese Stomatological Society*, **64**, pp. 314–319.
- [9] Verleg, M., 2015. "Wrist prosthesis: New two degrees-of-freedom hydraulic wrist mechanism for hand prostheses".
- [10] Cammarata, A., 2015. "Optimized design of a large-workspace 2-dof parallel robot for solar tracking systems". *Mechanism and Machine Theory*, **83**, 1, pp. 175–186.
- [11] Duan, X., Yang, Y., and Cheng, B., 2016. "Modeling and analysis of a 2-dof spherical parallel manipulator". *Sensors 2016, Vol. 16, Page 1485*, **16**, 9, p. 1485.
- [12] Sanchez, D., 2006. Surgical instrument with a universal wrist, 10. US Patent 7,121,781.
- [13] Wiitala, J. M., and Staniš, M. M., 2000. "Design of an over-

- constrained and dextrous spherical wrist”. *J. Mech. Des.*, **122**, pp. 347–353.
- [14] Lymark, H., and Mohl, F., 1966. An electromechanical forearm and hand.
- [15] Roose, C., 2014. Two-degree-of-freedom pneumatically powered wrist prosthesis.
- [16] Takeda, H., Tsujiuchi, N., Koizumi, T., Kan, H., Hirano, M., and Nakamura, Y., 2009. “Development of prosthetic arm with pneumatic prosthetic hand and tendon-driven wrist”. *Proceedings of the 31st Annual International Conference of the IEEE Engineering in Medicine and Biology Society: Engineering the Future of Biomedicine, EMBC 2009*, pp. 5048–5051.
- [17] Scarcia, U., Melchiorri, C., and Palli, G., 2015. “Towards simplicity: On the design of a 2-dofs wrist mechanism for tendon-driven robotic hands”. *2015 IEEE International Conference on Robotics and Biomimetics, IEEE-ROBIO 2015*, pp. 1317–1322.
- [18] Burbank, W. A., 2014. Four-cable wrist with solid surface cable channels, 9. US Patent 8,821,480.
- [19] Manzo, S., and Heaton, L., 2013. Wristed robotic surgical tool for pluggable end-effectors, 3. US Patent 8,398,634.
- [20] Wang, J., and Barry, O., 2020. “Multibody analysis and control of a full-wrist exoskeleton for tremor alleviation”. *Journal of Biomechanical Engineering*.
- [21] Kaufmann, R., Pfaeffle, J., Blankenhorn, B., Stabile, K., Robertson, D., and Goitz, R., 2005. “Kinematics of the midcarpal and radiocarpal joints in radioulnar deviation: an in vitro study”. *The Journal of hand surgery*, **30**(5), pp. 937–942.
- [22] Kaufmann, R. A., Pfaeffle, H. J., Blankenhorn, B. D., Stabile, K., Robertson, D., and Goitz, R., 2006. “Kinematics of the midcarpal and radiocarpal joint in flexion and extension: an in vitro study”. *The Journal of hand surgery*, **31**(7), pp. 1142–1148.
- [23] Rainbow, M. J., Kamal, R. N., Leventhal, E., Akelman, E., Moore, D. C., Wolfe, S. W., and Crisco, J. J., 2013. “In vivo kinematics of the scaphoid, lunate, capitate, and third metacarpal in extreme wrist flexion and extension”. *The Journal of hand surgery*, **38**(2), pp. 278–288.
- [24] Kane, T. R., and Levinson, D. A., 1985. “Dynamics, theory and applications”. p. 379.
- [25] Wang, J., and Barry, O. R., 2021. “Inverse optimal robust adaptive controller for upper limb rehabilitation exoskeletons with inertia and load uncertainties”. *IEEE Robotics and Automation Letters*, **6**, 4, pp. 2171–2178.
- [26] Wang, J., Kamidi, V. R., and Ben-Tzvi, P., 2018. “A multibody toolbox for hybrid dynamic system modeling based on nonholonomic symbolic formalism”. In *ASME 2018 Dynamic Systems and Control Conference*, American Society of Mechanical Engineers, pp. V003T29A003–V003T29A003.